https://doi.org/10.1016/j.enconman.2017.06.089

Application of cascading thermoelectric generator and cooler for waste heat recovery from solid oxide fuel cells

Houcheng Zhang [a, b, *], Wei Kong [a, c], Feifei Dong [a], Haoran Xu [a], Bin Chen [a], Meng Ni [a, *]

[a] *Department of Building and Real Estate, The Hong Kong Polytechnic University, Hong Kong, China*

[b] *Department of Microelectronic Science and Engineering, Ningbo University, Ningbo 315211, China*

[c] *School of Energy and Power Engineering, Jiangsu University of Science and Technology, Zhenjiang 212003, China*

Abstract: Besides electricity generation, solid oxide fuel cells (SOFCs) produce a significant amount of waste heat, which needs to be immediately removed to ensure durable operation of SOFCs. However, the removal of waste heat greatly decreases the efficiency of SOFCs. In this study, a new hybrid system mainly consisting of a thermoelectric generator, a thermoelectric cooler and an SOFC is proposed to recover the waste heat from SOFC for performance enhancement. The thermodynamic and electrochemical irreversible losses in each component are fully considered. An analytical relationship between the SOFC operating current density and the thermoelectric devices dimensionless electric current is derived, from which the range of SOFC operating current density that permits the thermoelectric devices to effectively work is determined. The equivalent power output and efficiency for the hybrid system are specified under different operating current density regions. The feasibility and effectiveness are illustrated by comparing the proposed hybrid system with the stand-alone SOFC. It is found that the power density and efficiency of the proposed system allow 2.3% and 4.6% larger than that of the stand-alone SOFC, respectively. Finally, various parametric analyses are performed to discuss the effects of some design and operation parameters on the hybrid system performance.

Key Words: Solid oxide fuel cell; thermoelectric generator; thermoelectric cooler; waste heat recovery; parametric study

*Corresponding authors.

Emails: zhanghoucheng@nbu.edu.cn (H. Zhang); bsmengni@polyu.edu.hk (M. Ni).

1. **Introduction**

The worldwide energy and environment crisis raise a strong demand for development of efficient and clean energy technologies [1]. Fuel cells are promising power sources as they can efficiently and environmental-friendly convert the fuel chemical energy into electricity without intermediary complicated energy conversion processes [2]. Among various fuel cells, SOFCs have attracted considerable interests due to their low emissions, fuel flexibility, inexpensive metal catalyst and high electrochemical reaction rate [3-5]. In literatures, a great number of studies have focused attention on aspects such as new electrode material fabrication [6, 7], lowering operating temperature [8, 9], durability improvement [10, 11], new cell prototype development [12, 13], and single cell theoretical modeling [14-16].

The high operating temperature of SOFCs also produces substantial amounts of high-grade heat that are capable of powering a wide range of bottoming thermodynamic devices [17-21]. By developing cogeneration or trigeneration systems, the energy and exergy efficiencies of SOFC-based hybrid systems could reach 80% and 60%, respectively [22-24]. Extensive studies have been conducted on SOFC-based hybrid systems fueled with various kinds of fuels [25-27] and integrated with different bottom cycles [28-32] by means of various analysis approaches [33-35]. Liao et al. proposed thermophotovoltaic cells to efficiently exploit the waste heat from SOFCs and compared the proposed hybrid system with some other SOFC based hybrid systems [28]. Mehrpooya et al. [29] introduced a combined system containing SOFC-GT (SOFC-gas turbine) system, steam Rankine cycle and absorption refrigeration system. They used energy and exergy as well as economic factors to discriminate optimum operation points of the combined system. Ma et al. [30] carried out thermodynamic analyses of a trigeneration system by employing an ammonia-water mixture thermodynamic cycle to harvest the waste heat from a natural gas fueled SOFC-GT. They examined the dependence of system performance on several important thermodynamic parameters. Ebrahimi et al. [31] proposed a novel cycle combining SOFC, micro gas turbine (MGT), and organic Rankine cycle (ORC) for power production. They evaluated the cycle behavior and investigated the effects of ten design parameters on the overall cycle electrical efficiency. Eveloy et al. [32] integrated a hybrid SOFC-GT system and a reverse osmosis plant to enhance power generation and desalinate seawater. Compared with existing standard gas turbine cycle, the proposed system could improve the exergy efficiency by approximately 29% and simultaneously produce additional 494 m^3/h fresh water. Rokni et al. [33] performed thermodynamic and thermoeconomic analyses of a biomass gasified SOFC/Stirling heat engine hybrid system. It was found that a thermal efficiency of 0.424 LHV and a net electric capacity of 120 kW_e were obtained when the feedstock was 89.4 kg/h. Lee et al. [34] evaluated the environmental impacts associated with a SOFC-based combined heat and power (CHP) generation system. It was showed that in the total environmental impact of manufacturing, the SOFC stack accounted for 72% and the remaining balance-of-plant were responsible for the rest 28%. Aminyavari et al. [35] implemented exergetic, economic and environmental analyses on an internal-reforming SOFC-GT hybrid system integrated with a steam Rankine cycle. After multi-objective optimization procedures, the final optimum results demonstrated that the exergy efficiency and total cost rate were 65.11% and 0.1374 €/s, respectively.

Thermoelectric devices include three semiconductor thermoelectric systems that convert waste heat into electric power (i.e., thermoelectric generator, TEG) or convert electricity into thermal energy for heating (i.e., thermoelectric heat pump, THP) or cooling (i.e., thermoelectric cooler, TEC) [36, 37]. As thermoelectric devices are compact, quiet, environmental-friendly and highly reliable, they are widely used in solar energy conversion [38], electronic cooling [39], residential air conditioning [40], and waste heat recovery [41, 42]. As all-solid-state energy converters, thermoelectric devices are natural good choices to recover the waste heat from SOFCs. To date, some scholars have employed TEGs to harvest waste heat from high-temperature fuel cells such as molten carbonate fuel cell [43], phosphoric acid fuel cell [44] and SOFC [45] for additional power generation. However, no one has yet used thermoelectric devices to recover the waste heat from SOFCs for cooling production, which is usually needed in buildings.

In this work, we present a new hybrid system that uses cascading thermoelectric devices to recover the waste heat from hydrogen-fueled SOFCs for cooling applications. Based on electrochemistry and non-equilibrium thermodynamics, the primary irreversible losses of each component with the hybrid system are described. The integration characteristics between the SOFC and thermoelectric devices will be investigated. Analytical expressions for evaluating the hybrid system performance will be given, through which the generic performance characteristics are discussed in detail. The feasibility and effectiveness for the proposed system will be demonstrated by comparing with the stand-alone SOFCs. Furthermore, extensive parametric studies will be employed to reveal the sensitivity of the hybrid system performance to some design parameters and operating conditions.

2. System description

The proposed hybrid system consists of an SOFC, two thermoelectric devices and a regenerator, as shown in Fig. 1. The thermoelectric devices consist of a TEG and a TEC, and the regenerator absorbs the heat in the outlet exhaust products to preheats the inlet reactants from ambient temperature T_0 to the SOFC operating temperature T. The SOFC electrochemically converts the fuel chemical energy into electrical power and high-grade waste heat. One part of the waste heat, Q_H (J s^{-1}), is transferred from the SOFC at temperature T to the TEG for additional electrical power generation via the Seebeck effect, and the generated electricity is subsequently delivered to power the TEC, which extract heat, Q_C (J s^{-1}), from the cooled space at temperature T_C based on the Peltier effect. Another part of the waste heat, Q_R (J s^{-1}), is consumed to compensate the regenerative losses in the regenerator. The rest part of the waste heat, Q_L (J s^{-1}), is directly rejected to the environment. Q_1 and Q_2 are heat-transfer rates between the environment and the TEG and TEC, respectively.

For simplification, following assumptions are adopted [46-50]:

- SOFC and thermoelectric devices are in steady states;
- Operating temperature and operating pressure of the SOFC are constants and uniform ;
- Reactants are completely consumed in the SOFC;
- Newton’s law is used to describe the heat transfers within the system;
- Thermoelectric elements in TEG and TEC are identical;
- Geometric configurations of the thermoelectric devices are in the optimum form;
- Thermoelectric elements are insulated both electrically and thermally from their surroundings, except at reservoir-junction contacts;
- Electric current flows along the arm of a thermoelectric element;
- External heat-transfer irreversibilities between the thermoelectric devices and the heat reservoirs are neglected;
- Seebeck coefficient, thermal conductance, electrical resistance, and figure of merit of the thermoelectric devices are independent of temperature;

- Thompson effects in thermoelectric devices are neglected.

2.1. SOFC

The typical SOFC shown in Fig. 1 is made of Ni | YSZ | LSM with hydrogen as fuel and air as oxidant. The SOFC electrochemical performance is deteriorated by activation, concentration and ohmic overpotentials, which can be characterized by the Bulter-Volmer equation, dusty gas model and Ohm's law, respectively. Adopting the electrochemical model in previous papers [51, 52], the power output P_{SOFC} and efficiency η_{SOFC} for a SOFC are given by

$$P_{SOFC} = VI = jA\left(E - V_{act,a} - V_{act,c} - V_{con,a} - V_{con,c} - V_{ohm}\right), \qquad (1)$$

and

$$\eta_{SOFC} = \frac{P_{SOFC}}{-\Delta \dot{H}}, \qquad (2)$$

where

$$V_{act,l} = \frac{RT}{F}\sinh^{-1}\left(\frac{j}{2j_{0,l}}\right) = \frac{RT}{F}\ln\left[\frac{j}{2j_{0,l}} + \sqrt{\left(\frac{j}{2j_{0,l}}\right)^2 + 1}\right] \qquad (l = a,\ c), \qquad (3)$$

$$V_{con,a} = \frac{RT}{2F}\ln\left(\frac{1 + j/j_{l\mathrm{H_2O}}}{1 - j/j_{l\mathrm{H_2}}}\right), \qquad (4)$$

$$V_{con,c} = \frac{RT}{4F}\ln\left[\frac{C^0_{\mathrm{O_2}}}{C_{T,c}/\delta_{\mathrm{O_2}} + (C^0_{\mathrm{O_2}} - C_{T,c}/\delta_{\mathrm{O_2}})\exp\left(L_c jA\delta_{\mathrm{O_2}}/(4FC_{T,c}D^{eff}_{\mathrm{O_2}})\right)}\right], \qquad (5)$$

$$V_{ohm} = j\left(\frac{L_a}{\sigma_a} + \frac{L_c}{\sigma_c} + \frac{L_e}{\sigma_e}\right), \qquad (6)$$

$$j_{0,a} = \gamma_a \frac{72X[D_p - (D_p + D_s)\varepsilon]\varepsilon}{D_s^2 D_p^2(1 - \sqrt{1 - X^2})}\left(\frac{P_{\mathrm{H_2}}}{P_{ref}}\right)\left(\frac{P_{\mathrm{H_2O}}}{P_{ref}}\right)\exp\left(-\frac{E_{act,a}}{RT}\right), \qquad (7)$$

$$j_{0,c} = \gamma_c \frac{72X[D_p - (D_p + D_s)\varepsilon]\varepsilon}{D_s^2 D_p^2(1 - \sqrt{1 - X^2})}\left(\frac{P_{\mathrm{O_2}}}{P_{\mathrm{ref}}}\right)^{0.25}\exp\left(\frac{-E_{act,c}}{RT}\right), \qquad (8)$$

and

$$-\Delta \dot{H} = -I\Delta h/(2F)\,. \tag{9}$$

2.2. Thermoelectric devices

As shown in Fig. 1, the TEG and TEC are operated between the heat sink (i.e., the ambience) and the SOFC and the cooled space, respectively. The number of thermoelectric elements in TEG and TEC are m and n, respectively, and the thermoelectric elements are electrically connected in serials. Each element consists of a P-type semiconductor leg and an N-type semiconductor leg which are connected by a thin copper. Neglecting the Thomson effect, the internal irreversible losses inside a thermoelectric element are mainly from the Joule heat and the heat-conduction losses between the hot junction and cold junction. The Joule heat generates an amount of heat $I_g^2 R_{te}$, where I_g is the electrical current flowing through a thermoelectric element, and R_{te} is the internal electrical resistance of a thermoelectric element. The heat-conduction losses in TEG and TEC are, respectively, $mK(T-T_0)$ and $nK(T_0-T_C)$, where K is the thermal conductance of a thermoelectric element. Based on the non-equilibrium thermodynamics, the heat balance equations can be expressed as [47]

$$Q_H = \alpha m I_g T - 0.5 m I_g^2 R_{te} + mK(T-T_0)\,, \tag{10}$$

$$Q_1 = \alpha m I_g T_0 + 0.5 m I_g^2 R_{te} + mK(T-T_0)\,, \tag{11}$$

$$Q_2 = \alpha n I_g T_0 + 0.5 n I_g^2 R_{te} - nK(T_0-T_C)\,, \tag{12}$$

and

$$Q_C = \alpha n I_g T_C - 0.5 n I_g^2 R_{te} - nK(T_0-T_C)\,, \tag{13}$$

where α_P, α_N and $\alpha = (\alpha_P - \alpha_N)$ are the Seebeck coefficients of a P-type semiconductor leg, an N-type semiconductor leg and a thermoelectric element, respectively.

Based on Eqs. (10) - (13), one may define an internal structure parameter x to describe the ratio of thermoelectric element numbers between the TEG and the TEC, i.e.,

$$x = m/n = \frac{1-\tau_2 + i/(ZT_0)}{1/\tau_1 - 1 - i/(ZT_0)}, \tag{14}$$

where $\tau_1 = T_0/T$, $\tau_2 = T_C/T_0$, $\tau = \tau_1\tau_2 = T_C/T$, $i = \alpha I_g/K$ and $Z = \alpha^2/(KR_{te})$ are dimensionless electric current and figure of merit of a thermoelectric element, respectively.

From Eqs. (10) – (14), the coefficient of performance (COP) ψ and the cooling rate (CR) Φ of the cascading thermoelectric devices can be, respectively, expressed as

$$\psi = \frac{Q_C}{Q_H} = \frac{\left[i\tau_2 - i^2/(2ZT_0) - 1 + \tau_2\right]\left[1-\tau_1 - i\tau_1/(ZT_0)\right]}{\left[i - i^2/(2ZT_0) + 1 - \tau_1\right]\left[1-\tau_2 + i/(ZT_0)\right]}, \tag{15}$$

and

$$\Phi = Q_C = Km(1+1/x)T_0 \frac{\left[i\tau_2 - i^2/(2ZT_0) - 1 + \tau_2\right]\left[1-\tau_1 - i\tau_1/(ZT_0)\right]}{1-\tau}. \tag{16}$$

When the thermoelectric devices begin to work, both the COP and the CR are larger than zero, i.e., $\psi > 0$ and $\Phi > 0$. Solving the inequalities, the effective dimensionless electric current range is given by

$$i_1 < i < i_2, \tag{17}$$

where $i_1 = ZT_0\tau_2\left[1 - \sqrt{1 - 2(1-\tau_2)/(ZT_0\tau_2^2)}\right]$ and $i_2 = ZT_0(1/\tau_1 - 1)$. Substituting i_1 and i_2 into Eq. (14), the corresponding internal structure parameters are $x_1 = \left(\tau_1 - \tau\sqrt{1 - 2(1-\tau_2)/(ZT_0\tau_2^2)}\right) \Big/ \left[1 - \tau_1 - \left(1 - \sqrt{1 - 2(1-\tau_2)/(ZT_0\tau_2^2)}\right)\tau\right]$ and $x_2 \to \infty$, respectively. To make the thermoelectric devices effective, the internal structure parameter of the thermoelectric devices should be designed as

$$x > x_1. \tag{18}$$

Considering the exergy content difference between the cooling load and the electric power [53], the equivalent power output P_{te} and efficiency η_{te} for the cascading thermoelectric devices can be expressed as

$$P_{td} = Q_C \left|1 - T_0/T_C\right| = KT_0 m\left(1 + 1/x\right)\left|1 - T_0/T_C\right| \frac{\left[i\tau_2 - i^2/\left(2ZT_0\right) - 1 + \tau_2\right]\left[1 - \tau_1 - i\tau_1/\left(ZT_0\right)\right]}{\left(1 - \tau\right)}, \tag{19}$$

and

$$\eta_{td} = \frac{P_{td}}{Q_H} = KT_0 m\left(1 + 1/x\right)\left|1 - T_0/T_C\right| \frac{\left[i\tau_2 - i^2/\left(2ZT_0\right) - 1 + \tau_2\right]\left[1 - \tau_1 - i\tau_1/\left(ZT_0\right)\right]}{\left(1 - \tau\right)Q_H}. \tag{20}$$

2.3. Regenerator

The thermodynamic losses in the regenerator are often expressed as [54]:

$$Q_R = K_{re} A_{re} (1 - \beta)(T - T_0), \tag{21}$$

where K_{re}, A_{re} and β are the heat-transfer coefficient, heat-transfer area and the effectiveness of the regenerator, respectively.

2.4. Performance of the hybrid system

The heat leakage rate Q_L between the SOFC and the environment can be described by [54]

$$Q_L = K_L A_L (T - T_0), \tag{22}$$

where K_L and A_L are the heat leakage coefficient and area, respectively.

According to the energy conservation law, one has

$$Q_H = -\Delta \dot{H} - P_{SOFC} - Q_R - Q_L = -\frac{A\Delta h}{2F}\left[\left(1 - \eta_{SOFC}\right) j - \frac{2Fc_1\left(T - T_0\right)}{-\Delta h} - \frac{2Fc_2\left(T - T_0\right)}{-\Delta h}\right], \tag{23}$$

where $c_1 = K_{re} A_{re} (1 - \xi)/A$ and $c_2 = K_L A_L / A$ are temperature-independent composite constants which are associated with the regenerative losses and the heat leakage, respectively.

Based on Eqs. (10) and (23), the numerical relationship between the dimensionless electric current of the thermoelectric devices, i, and the operating current density of SOFC, j, is determined by Eq. (24)

$$i = ZT - \sqrt{Z^2T^2 + 2Z(T - T_0) - \frac{ZA}{mK}\left[\frac{-\Delta h}{F}(1-\eta_{SOFC})j - 2(c_1 + c_2)(T - T_0)\right]}. \quad (24)$$

Using Eqs. (14) and (24) and the parameters given in Table 1 [43, 49, 51, 52, 55], one can generate the curves of $x \sim j$ for different T_C and T_0, as shown in Fig. 2 (a). It is seen that x first smoothly and then sharply increases with increasing j, and x increases as T_C decreases or T_0 increases. Compared with the variation of T_C, x is more sensitive to the variation of T_0. Fig. 2 (b) shows the equivalent power density varying with the equivalent efficiency of the thermoelectric devices at different T_0 or T_C. $P^*_{td,\max}$, $\eta_{td,\max}$, $P^*_{td,\eta}$ and $\eta_{td,P}$ move towards larger ones as T_C decreases or T_0 increases. In a word, the thermoelectric devices display better performance under the larger temperature gap $(T_0 - T_C)$ condition.

Replacing the symbol i in Eq. (24) by the i_1 and i_2 in Eq. (17) respectively, one may numerically determine the lower bound j_1 and upper bound j_2 between which the thermoelectric devices enable to work. Thus, the effective operating current density interval is given by

$$\Delta j = j_2 - j_1. \quad (25)$$

Thus, the overall equivalent power output P and efficiency η for the proposed hybrid system can be, respectively, given by

$$P = \begin{cases} = P_{SOFC} + P_{td} & (j_1 < j < j_2) \\ = P_{SOFC} & (j \le j_1 \;\; or \;\; j \ge j_2) \end{cases} \quad (26)$$

and

$$\eta = \begin{cases} = \dfrac{P_{SOFC} + P_{td}}{-\Delta \dot{H}} & (j_1 < j < j_2) \\ = \eta_{SOFC} & (j \le j_1 \;\; or \;\; j \ge j_2) \end{cases} \quad (27)$$

3. Generic performance characteristics

Figure 3 shows the generic performance characteristics and comparisons between the SOFC and the thermoelectric devices and the proposed hybrid system. It is seen that P^*_{SOFC}, P^*_{td} and P^* first increase and then decrease as j increases. Different from the trends of power densities, η_{SOFC} continuously decreases as j increases in the entire range, while η_{td} first increases and then decreases in the region of $j_1 < j < j_2$, and η first quickly decreases then somewhat increases and finally drops as j increases. Outside the region of $j_1 < j < j_2$, the curves of $P^* \sim j$ and $\eta \sim j$ are respectively overlapped with that of $P^*_{SOFC} \sim j$ and $\eta_{SOFC} \sim j$, and the values of P^*_{td} and η_{td} are equal to 0. It is also observed that $P^*_{\max}$ is larger than both $P^*_{SOFC,\max}$ and $P^*_{td,\max}$, and η_P is larger than $\eta_{SOFC,P}$. For the parameters in Table 1, $P^*_{\max}$ is about 2.3% larger than $P^*_{SOFC,\max}$, and η_P is about 4.6% larger than $\eta_{SOFC,P}$. Compared with the stand-alone SOFC, the performance improvement of the proposed hybrid system is not adequately obvious. This is because the heat-electricity efficiency of TEGs is relatively low and a large exergy destruction occurs in the cooling processes. Moreover, j_P is always different from $j_{fc,P}$ because P^*_{SOFC} and P^*_{td} achieve their peak values at different operating current densities. Combining the power output and efficiency criteria, the optimum operating ranges for current density, power density and efficiency are suggested to be located in $j \le j_P$, $P^* \le P^*_{\max}$ and $\eta \ge \eta_P$, respectively.

4. Parametric studies

4.1. Effect of m

A larger m indicates more thermoelectric elements are employed in TEG and TEC, which facilitates the performance improvement of the thermoelectric devices. As shown in Fig. 4 (a), $P^*_{td,\max}$, $j_{td,P}$, $j_{td,\eta}$, j_1, j_2 and Δj increase while $\eta_{td,\max}$ almost keeps invariant as m

increases, and curves of $P_{td}^{*} \sim j$ and $\eta_{td} \sim j$ move rightward with increasing m. For the hybrid system, the effects of m are only in the region of $j_1 < j < j_2$, as shown in Fig. 4 (b). It is interesting to note that $P_{\max}^{*}$ first increases and then decrease with the increasing m, and consequently, there exists an optimum value for m at which $P_{\max}^{*}$ attains its maximum. This is because the increase in P_{td}^{*} is less significantly than the decrease in P_{SOFC}^{*} for a larger m at which $j_{td,P}$ exceeds $j_{SOFC,P}$. For parameters in Table 1, an optimum value for m is located between 8 and 12.

4.2. Effect of T

A higher operating temperature T not only improves the performances of the SOFC and the thermoelectric devices but also leads to larger thermodynamic losses within the system. Because the performance deterioration caused by the thermodynamic losses is less significant than the performance improvements in the SOFC and thermoelectric devices, a higher operating temperature is desired. As shown in Fig. 5, P^{*} and η increase with increasing T, and the values of j_P, j_S, j_1, j_2 and Δj increase with increasing T. The effect of T occurs in the whole range of j and becomes more significantly at elevated T. However, a larger T would cause some problems such as performance degradation, slow start-up and shutdown cycles and higher costs for balance of plant (BOP). Lowing the operating temperature of SOFCs to the intermediate temperature range (500–700°C) has become an important topic in SOFC community [56].

4.3. Effects of p

Operating pressure not only affects the SOFC performance (via open circuit potential and overpotentials) but also influences the waste heat quantity transferred to the thermoelectric devices. Similar to T, the effects of operating pressure p on the system performance is in the whole region of j. Figure 6 shows that both P^* and η increase with increasing p, and the values of $P^*_{\max}$, $P^*_{SOFC,\max}$, j_P, j_S, j_1, j_2 and $\Delta \boldsymbol{j}$ are also increased with increasing p. The effect of p on the system performance becomes more significantly at larger operating current densities. For performance improvement, a larger p is always more preferable, but it also consumes some additional electricity in the inlet reactants compression processes. The black solid lines in Fig. 6 represents the operating pressure is chosen as 1.0 atm, which is the usual choice in practice.

4.4. Effects of K

Thermal conductance K significantly affects the thermoelectric devices performance, as shown in Fig. 7 (a). Similar to the effects of m, $P^*_{td,\max}$, $j_{td,P}$, $j_{td,\eta}$, j_1, j_2 and Δj increase while $\eta_{td,\max}$ almost keeps invariant as K increases, and the curves of $P^*_{td} \sim j$ and $\eta_{td} \sim j$ move rightward with increasing m. Different from T and p, Figure 7 (b) shows that the effects of K on the whole system performance are only in the region of $j_1 < j < j_2$. Outside this region, the curves of $P^* \sim j$ and $\eta \sim j$ are overlapped with that of the $P^*_{SOFC} \sim j$ and $\eta_{SOFC} \sim j$, respectively. The value of $P^*_{\max}$ first increases and then decreases with increasing K, while the value of j_P continuously increases as K increases. At a small K, P^*_{td} is much smaller than P^*_{SOFC} such that the whole system performance improvement is not obvious. As K increases, the increase in P^*_{td} is less significantly than the decrease in P^*_{SOFC}, especially for the cases of $j_{td,P} > j_{SOFC,P}$. For the parameters in Table 1, an optimum value for K is found to be between 0.04 and 0.08.

4.5. Effects of c_1 / c_2

The integrated parameters c_1 and c_2 are closely related with the thermodynamic losses within the hybrid system. As shown in Fig. 8, the value of $P^*_{\max}$ almost keeps invariant for small c_1 and

c_2, and the effects of c_1 and c_2 only occur in the region of $j_1 < j < j_2$. As c_1 and/or c_2 increase, the value of $P^*_{\max}$ drops evidently, especially for the cases of $j_{td,P} > j_{SOFC,P}$. It is also seen that the values of j_P, j_1 and j_2 are increased as c_1 and/or c_2 are increased. Numerical calculations further show that the value of Δj slightly decreases as c_1 and/or c_2 increase. The black solid lines in Fig. 8 represent a special case that both regenerative losses Q_R and heat leakage Q_L are negligible. In such a situation, Eqs. (23) and (24) can be, respectively, simplified into

$$Q_H = -\frac{jA\Delta h}{2F}\left(1-\eta_{SOFC}\right), \tag{28}$$

and

$$i = ZT - \sqrt{Z^2T^2 + 2Z\left(T-T_0\right) - \frac{ZA}{mK}\left[\frac{-\Delta h}{F}\left(1-\eta_{SOFC}\right)j\right]}. \tag{29}$$

4. Conclusions

A novel hybrid system consisting of SOFCs and cascading thermoelectric devices is proposed to recover waste heat from SOFCs for simultaneous power generation and cooling applications. A theoretical model is derived to evaluate the hybrid system performance, considering various irreversible losses in the system. A numerical relationship for the output electric currents of the SOFC and the cascading thermoelectric devices is derived, and the current density interval of SOFC that allows the thermoelectric devices to work is determined. The internal structure parameter x and equivalent power density and efficiency of the thermoelectric devices varying with the heat reservoir temperatures are revealed. The performance parameters for the hybrid system are specified under different operating conditions, and the generic performance characteristics are demonstrated. Numerical calculations show that the power density and efficiency of the proposed system allow 2.3% and 4.6% larger than that of the stand-alone SOFC, respectively. Comprehensive parametric studies are conducted to discuss the effects of some design and operation parameters on the hybrid system performance. It is found that there exist optimum values for the number of thermoelectric elements in TEG and the thermal conductance of a thermoelectric element for maximizing the hybrid system equivalent power density.

Acknowledgments

This work has been supported by the National Natural Science Foundation of China (Grant No. 51406091) , and The Hong Kong Polytechnic University Research Project (Grant No. 1-YW1F).

References

[1] Panwar NL, Kaushik SC, Kothari S. Role of renewable energy sources in environmental protection: a review. Renew Sust Energ Rev 2011; 15: 1513-24.

[2] Lucia U. Overview of fuel cells. Renew Sust Energ Rev 2014; 30: 164-9.

[3] Mekhilef S, Saidur R, Safari A. Comparative study of different fuel cell technologies. Renew Sust Energ Rev 2012; 16: 981-9.

[4] Choudhury A, Chandra H, Arora A. Application of solid oxide fuel cell technology for power generation—A review. Renew Sust Energ Rev 2013; 20: 430-42.

[5] Dong F, Ni M, He W, Chen Y, Yang G, Chen D, Shao Z. An efficient electrocatalyst as cathode material for solid oxide fuel cells: $BaFe_{0.95}Sn_{0.05}O_{3-\delta}$. J Power Sources 2016; 326: 459-65.

[6] Sengodan S, Choi S, Jun A, Shin TH, Ju YW, Jeong HY, et al. Layered oxygen-deficient double perovskite as an efficient and stable anode for direct hydrocarbon solid oxide fuel cells. Nat Mat 2015; 14: 205-9.

[7] Mahato N, Banerjee A, Gupta A, Omar S, Balani K. Progress in material selection for solid oxide fuel cell technology: A review. Prog Mat Sci 2015; 72: 141-337.

[8] Huang J, Xie F, Wang C, Mao Z. Development of solid oxide fuel cell materials for intermediate-to-low temperature operation. Int J Hydrogen Energy 2012; 37: 877-83.

[9] Recent progress on solid oxide fuel cell: Lowing temperature and utilizing non-hydrogen fuels. Int J Hydrogen Energy 2013; 38: 16498-517.

[10] Lanzini A, Leone P, Guerra C, Smeacetto F, Brandon NP, Santarelli M. Durability of anode supported Solid Oxide Fuel Cells (SOFC) under direct dry-reforming of methane. Chem Eng J 2013; 220: 254-63.

[11] Sumi H, Yamaguchi T, Suzuki T, Shimada H, Hamamoto K, Fujishiro Y. Effects of anode microstructures on durability of microtubular solid oxide fuel cells during internal steam reforming of methane. Electrochem Commun 2014; 49: 34-7.

[12] Fan L, Su PC. Layer-structured $LiNi_{0.8}Co_{0.2}O_2$: A new triple (H^+ /O^{2-} /e^-) conducting cathode for low temperature proton conducting solid oxide fuel cells. J Power Sources 2016; 306: 369-77.

[13] Huang K, Singhal SC. Cathode-supported tubular solid oxide fuel cell technology: A critical review. J Power Sources 2013; 237: 84-97.

[14] He W, Zou J, Wang B, Vilayurganapathy S, Zhou M, Lin X, et al. Gas transport in porous electrodes of solid oxide fuel cells: A review on diffusion and diffusivity measurement. J Power Sources 2013; 237: 64-73.

[15] Bertei A, Nicolella C. Common inconsistencies in modeling gas transport in porous electrode: The dusty-gas model and the Fick's law. J Power Sources 2015; 279: 133-7.

[16] Abdeljawad F, Volker B, Davis R, McMeeking RM, Haataja M. Connecting microstructural coarsening processes to electrochemical performance in solid oxide fuel cells: An integrated modeling approach. J Power Sources 2014; 250: 319-31.

[17] McLarty D, Brouwer J, Samuelsen S. Fuel cell–gas turbine hybrid system design part I: Steady state performance. J Power Sources 2014; 257: 412-20.

[18] Rokni M. Thermodynamic analysis of SOFC (solid oxide fuel cell)–Stirling hybrid plants using alternative fuels. Energy 2013; 61: 87-97.

[19] Rokni M. Biomass gasification integrated with a solid oxide fuel cell and Stirling engine. Energy 2014; 77: 6-18.

[20] Buonomano A, Calise F, d'Accadia MD, Palombo A, Vicidomini M. Hybrid solid oxide fuel

cells–gas turbine systems for combined heat and power: a review. Appl Energy 2015; 156: 32-85.

[21] Zhang X, Chan SH, Li G,Ho HK, Li J, Feng Z. A review of integration strategies for solid oxide fuel cells. J Power Sources 2010; 195: 685-702.

[22] Khani L, Mahmoudi SMS, Chitsaz A, Rosen MA. Energy and exergoeconomic evaluation of a new power/cooling cogeneration system based on a solid oxide fuel cell. Energy 2016; 94: 64-77.

[23] Tippawan P, Arpornwichanop A, Dincer I. Energy and exergy analyses of an ethanol-fueled solid oxide fuel cell for a trigeneration system. Energy 2015; 87: 228-39.

[24] Ranjbar F, Chitsaz A, Mahmoudi SMS, Khalilarya S, Rosen MA. Energy and exergy assessments of a novel trigeneration system based on a solid oxide fuel cell. Energy Convers Managem 2014; 87: 318-27.

[25] Gholamian E, Zare V, Mousavi SM. Integration of biomass gasification with a solid oxide fuel cell in a combined cooling, heating and power system: A thermodynamic and environmental analysis. Int J Hydrogen Energy 2016; 41: 20396-406.

[26] Lv X, Gu C, Liu X, Weng Y. Effect of gasified biomass fuel on load characteristics of an intermediate-temperature solid oxide fuel cell and gas turbine hybrid system. Int J Hydrogen Energy 2016; 41: 9563-76.

[27] Borji M, Atashkari K, Ghorbani S, Nariman-Zadeh N. Parametric analysis and Pareto optimization of an integrated autothermal biomass gasification, solid oxide fuel cell and micro gas turbine CHP system. Int J Hydrogen Energy 2015; 40: 14202-23.

[28] Liao T, Cai L, Zhao Y, Chen J. Efficiently exploiting the waste heat in solid oxide fuel cell by means of thermophotovoltaic cell. J Power Sources 2016; 306: 666-73.

[29] Mehrpooya M, Dehghani H, Moosavian SMA. Optimal design of solid oxide fuel cell,

ammonia-water single effect absorption cycle and Rankine steam cycle hybrid system. J Power Sources 2016; 306: 107-23.

[30] Ma S, Wang J, Yan Z, Dai Y, Lu B. Thermodynamic analysis of a new combined cooling, heat and power system driven by solid oxide fuel cell based on ammonia–water mixture. J Power Sources 2011; 196: 8463-71.

[31] Ebrahimi M, Moradpoor I. Combined solid oxide fuel cell, micro-gas turbine and organic Rankine cycle for power generation (SOFC–MGT–ORC). Energy Convers Managem 2016; 116: 120-33.

[32] Eveloy V, Rodgers P, Qiu L. Integration of an atmospheric solid oxide fuel cell-gas turbine system with reverse osmosis for distributed seawater desalination in a process facility. Energy Convers Managem 2016; 126: 944-59.

[33] Rokni M. Thermodynamic and thermoeconomic analysis of a system with biomass gasification, solid oxide fuel cell (SOFC) and Stirling engine. Energy 2014; 76: 19-31.

[34] Lee YD, Ahn KY, Morosuk T, Tsatsaronis G. Environmental impact assessment of a solid-oxide fuel-cell-based combined-heat-and-power-generation system. Energy 2015; 79: 455-466.

[35] Aminyavari M, Mamaghani A H, Shirazi A, Najafi B, Rinaldi F. Exergetic, economic, and environmental evaluations and multi-objective optimization of an internal-reforming SOFC-gas turbine cycle coupled with a Rankine cycle. Appl Therm Eng 2016; 108: 833-46.

[36] Bell LE. Cooling, heating, generating power, and recovering waste heat with thermoelectric systems. Science 2008; 321: 1457-61.

[37] Elsheikh MH, Shnawah DA, Sabri MFM, Said SBM, Hassan MH, Bashir MB, et al. A review on thermoelectric renewable energy: Principle parameters that affect their performance. Renew Sust

Energ Rev 2014; 30: 337-55.

[38] Moraes FS, Santos LC, Alencar RN, Alencar RN, Sempels EV, Sandoval V SC, et al. Solar thermoelectric generator performance relative to air speed. Energy Convers Managem 2015; 99: 326-33.

[39] Ma M, Yu J. An analysis on a two-stage cascade thermoelectric cooler for electronics cooling applications. Int J Refrig 2014; 38: 352-57.

[40] Kim YW, Ramousse J, Fraisse G, Dalicieux P, Baranek P. Optimal sizing of a thermoelectric heat pump (THP) for heating energy-efficient buildings. Energy Build 2014; 70: 106-16.

[41] Sun X, Liang X, Shu G, Tian H, Wei H, Wang X. Comparison of the two-stage and traditional single-stage thermoelectric generator in recovering the waste heat of the high temperature exhaust gas of internal combustion engine. Energy 2014; 77: 489-98.

[42] Zhang H, Wang H, Zhu X, Qiu YJ, Li K, Chen R, et al. A review of waste heat recovery technologies towards molten slag in steel industry. Appl energy 2013; 112: 956-66.

[43] Wu S, Zhang H, Ni M. Performance assessment of a hybrid system integrating a molten carbonate fuel cell and a thermoelectric generator. Energy 2016; 112: 520-7.

[44] Chen X, Wang Y, Cai L, Zhou Y. Maximum power output and load matching of a phosphoric acid fuel cell-thermoelectric generator hybrid system. J Power Sources 2015; 294: 430-6.

[45] Chen X, Pan Y, Chen J. Performance and evaluation of a fuel cell-thermoelectric generator hybrid system. Fuel Cells 2010; 10: 1164-70.

[46] Chan SH, Khor KA, Xia ZT. A complete polarization model of a solid oxide fuel cell and its sensitivity to the change of cell component thickness. J Power Sources 2001; 93: 130-40.

[47] Chen L, Li J, Sun F, Wu C. Performance optimization of a two-stage semiconductor

thermoelectric-generator. Appl Energy 2005; 82: 300-12.

[48] Khattab NM, Shenawy ETE. Optimal operation of thermoelectric cooler driven by solar thermoelectric generator. Energy Convers Manag 2006; 47: 407-26.

[49] Chen X, Lin B, Chen J. The parametric optimum design of a new combined system of semiconductor thermoelectric devices. Appl Energy 2006; 83: 681-6.

[50] Chen WH, Wang CC, Hung CI. Geometric effect on cooling power and performance of an integrated thermoelectric generation-cooling system. Energy Convers Manag 2014; 87: 566-75.

[51] Ni M, Leung MKH, Leung DYC. Parametric study of solid oxide fuel cell performance. Energy Convers Manag 2007; 48: 1525-35.

[52] Zhang H, Chen J, Zhang J. Performance analysis and parametric study of a solid oxide fuel cell fueled by carbon monoxide. Int J Hydrogen Energy 2013; 38: 16354-64.

[53] Chen X, Wang Y, Zhou Y. Equivalent power output and parametric optimum design of a PEM fuel cell-based hybrid system. Int J Electr Power Energy Sys 2014; 63: 429-33.

[54] Zhao M, Zhang H, Hu Z, Zhang Z, Zhang J. Performance characteristics of a direct carbon fuel cell/thermoelectric generator hybrid system. Energy Convers Manag 2015; 89: 683-9.

[55] Liang X, Sun X, Tian H, Shu G, Wang Y, Wang X. Comparison and parameter optimization of a two-stage thermoelectric generator using high temperature exhaust of internal combustion engine. Appl Energy 2014; 130: 190-9.

[56] Wachsman ED, Lee KT. Lowering the temperature of solid oxide fuel cells. Science 2011; 334: 935-9.

Table captions:

Table 1. Parameters used in the modeling [43, 49, 51, 52, 55].

Figure captions:

Fig. 1. A conceptual diagram of an SOFC/ thermoelectric devices hybrid system.

Fig. 2. Curves of (a) $x \sim j$, and (b) $P_{td}^{*} \sim \eta_{td}$ at different T_0 or T_C, where $P_{td}^{*} = P_{td} / A$ is the equivalent power density of the thermoelectric devices, $P_{td,\max}^{*}$ and $\eta_{td,\max}$ are respectively the maximum power density and maximum efficiency of the thermoelectric devices, $P_{td,\eta}^{*}$ and $\eta_{td,P}$ are the power density at $\eta_{td,\max}$ and the efficiency at $P_{td,\max}^{*}$, respectively.

Fig. 3. Comparisons of (a) power densities and (b) efficiencies between the SOFC, thermoelectric devices and hybrid system, where $P_{SOFC}^{*} = P_{SOFC} / A$ and $P^{*} = P / A$ are, power densities for SOFC and hybrid system, respectively; $P_{SOFC,\max}^{*}$, $P_{td,\max}^{*}$ and $P_{\max}^{*}$ are maximum power densities of the SOFC, thermoelectric devices and hybrid system, respectively; $\eta_{td,\max}$ is the maximum efficiency of the thermoelectric devices; j_P and η_P are operating current density and efficiency at $P_{\max}^{*}$, respectively; $j_{fc,P}$ is the operating current density at $P_{SOFC,\max}^{*}$; $j_{td,P}$ and $j_{td,\eta}$ are operating current densities at $P_{td,\max}^{*}$ and $\eta_{td,\max}$, respectively; j_S is the stagnation current density from which the SOFC does not output electricity any more.

Fig. 4. Effects of the number of thermoelectric elements in TEG on the hybrid system performance.

Fig. 5. Effects of the operating temperature on the hybrid system performance.

Fig. 6. Effects of the operating pressure on the hybrid system performance.

Fig. 7. Effects of the thermal conductance of a thermoelectric element on the hybrid system performance.

Fig. 8. Effects of the thermodynamic losses related parameters on the hybrid system performance.

Table 1

Parameter	Value
Operating pressure, P (atm)	1.0
Operating temperature, T (K)	1073
Anode interface gas compositions	95 % H_2 +5 % H_2O
Cathode interface gas compositions	79 % N_2 +21% O_2
Activation energy for anode, E_{acta} (J mol^{-1})	1.0×10^5 [51]
Activation energy for cathode, E_{actc} (J mol^{-1})	1.2×10^5 [51]
Electrode porosity, ε	0.48 [51]
Electrode tortuosity, ξ	5.4 [51]
Average pore diameter, D_p (m)	3.0×10^{-6} [51]
Average grain size, D_s (m)	1.5×10^{-6} [51]
Average length of grain contact, X	0.7 [51]
Anode thickness , L_a (m)	5.0×10^{-4}
Anode electric conductivity, σ_a (Ω^{-1} m^{-1})	8.0×10^4 [52]
Cathode thickness, L_c (m)	5.0×10^{-5}
Cathode electric conductivity, σ_c (Ω^{-1} m^{-1})	8.4×10^3 [52]
Electrolyte thickness , L_e (m)	5.0×10^{-5}
Electrolyte ionic conductivity, σ_e (Ω^{-1} m^{-1})	$3.34\times10^4\exp(-1.03\times10^4/T)$ [52]
Effective surface area of the SOFC, A (m^2)	4.0×10^{-2}
Sectional area of a thermoelectric element, (m^2)	0.005 [55]
Heat conductivity of a thermoelectric element, K (W K^{-1} m^{-1})	0.04
Figure of merit of the thermoelectric materials, ZT_0	1.0 [49]
Number of TEGs, m	8
Constants in Eq. (23), c_1; c_2 (W m^{-2} K^{-1})	0.1; 0.1 [43]
Temperature of the ambience, T_0 (K)	305
Temperature of cooled space , T_C (K)	290

Fig. 1.

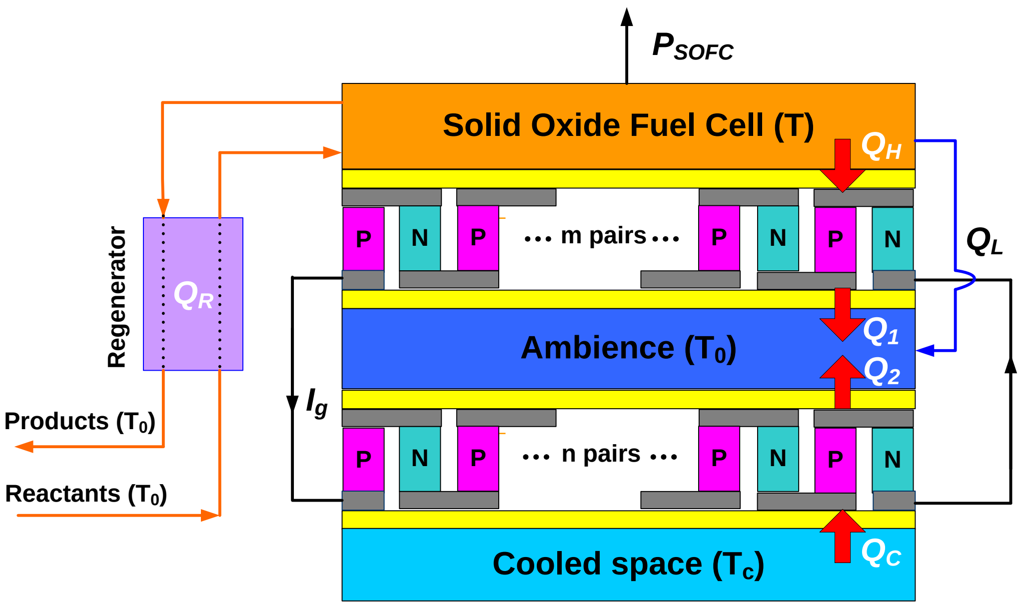

P_SOFC
Solid Oxide Fuel Cell (T)
Q_H
Q_L
Regenerator
Q_R
P
N
… m pairs …
Ambience (T_0)
Q_1
Q_2
I_g
… n pairs …
Products (T_0)
Reactants (T_0)
Cooled space (T_c)
Q_C

Fig. 2.

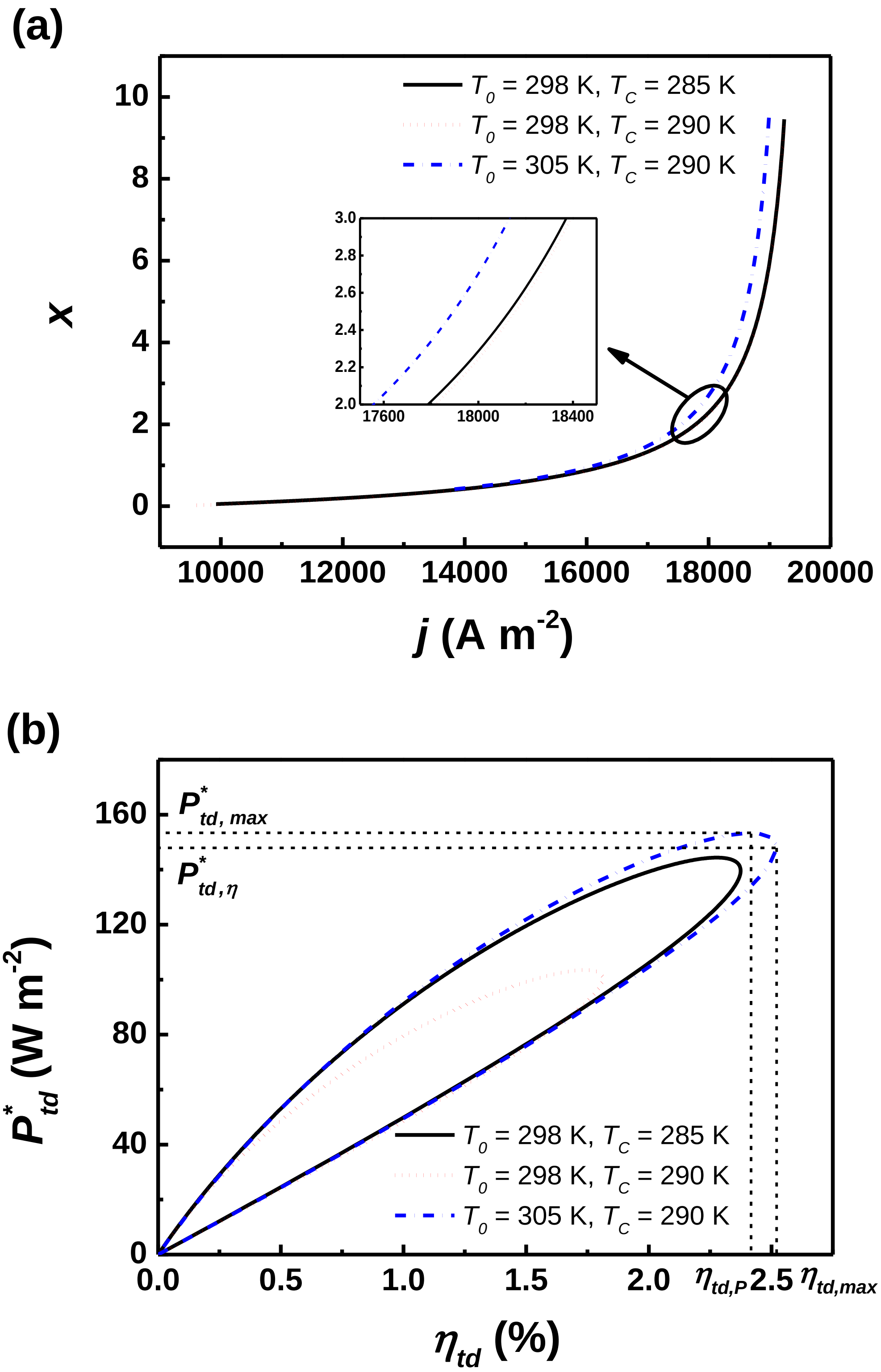

(a)
T0 = 298 K, TC = 285 K
T0 = 298 K, TC = 290 K
T0 = 305 K, TC = 290 K
x
j (A m-2)
(b)
P*td, max
P*td,η
P*td (W m-2)
ηtd (%)
ηtd,P
ηtd,max

Fig. 3.

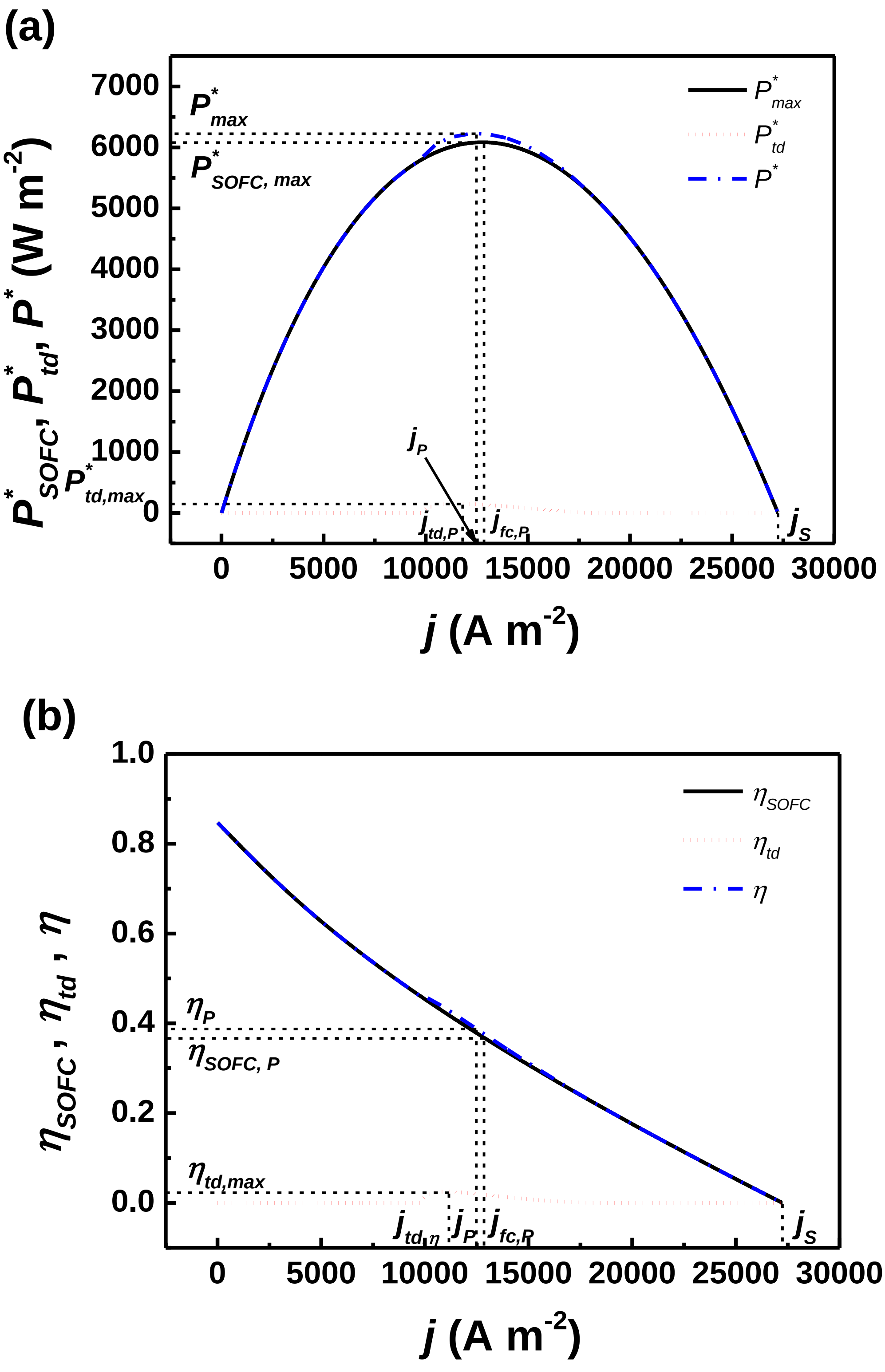
(a)
7000
6000
5000
4000
3000
2000
1000
0
P*max
P*SOFC, max
P*td,max
jP
jtd,P
jfc,P
jS
P*max
P*td
P*
P*SOFC, P*td, P* (W m-2)
0
5000
10000
15000
20000
25000
30000
j (A m-2)
(b)
1.0
0.8
0.6
0.4
0.2
0.0
ηP
ηSOFC, P
ηtd,max
jtd,η
jP
jfc,P
jS
ηSOFC
ηtd
η
ηSOFC , ηtd , η
0
5000
10000
15000
20000
25000
30000
j (A m-2)

Fig. 4.

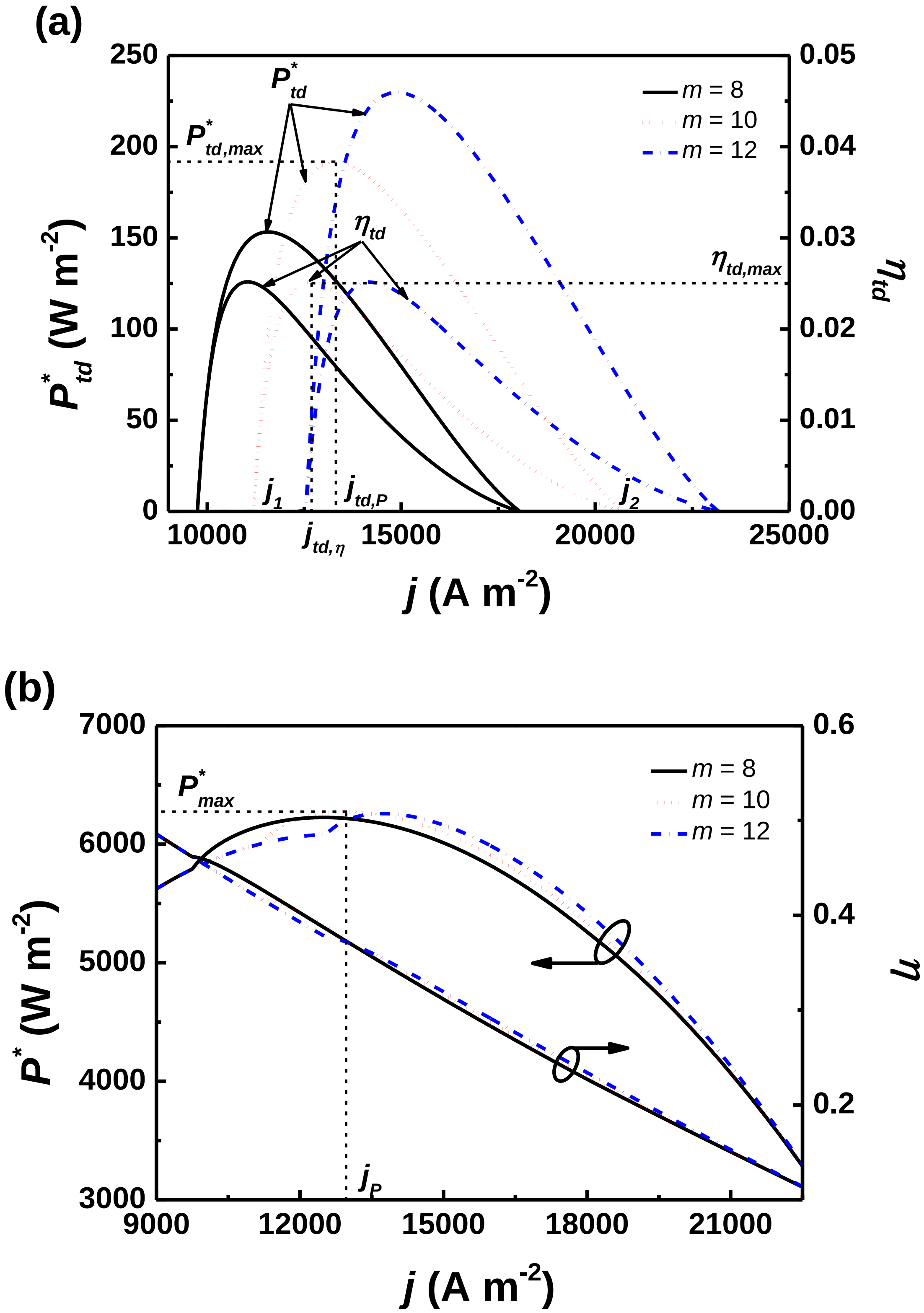
(a)
250
200
150
100
50
0
0.05
0.04
0.03
0.02
0.01
0.00
10000
15000
20000
25000
m = 8
m = 10
m = 12
P*td
P*td,max
ηtd
ηtd,max
j1
jtd,P
jtd,η
j2
P*td (W m-2)
ηtd
j (A m-2)
(b)
7000
6000
5000
4000
3000
0.6
0.4
0.2
9000
12000
15000
18000
21000
m = 8
m = 10
m = 12
P*max
jP
P* (W m-2)
η
j (A m-2)

Fig. 5.

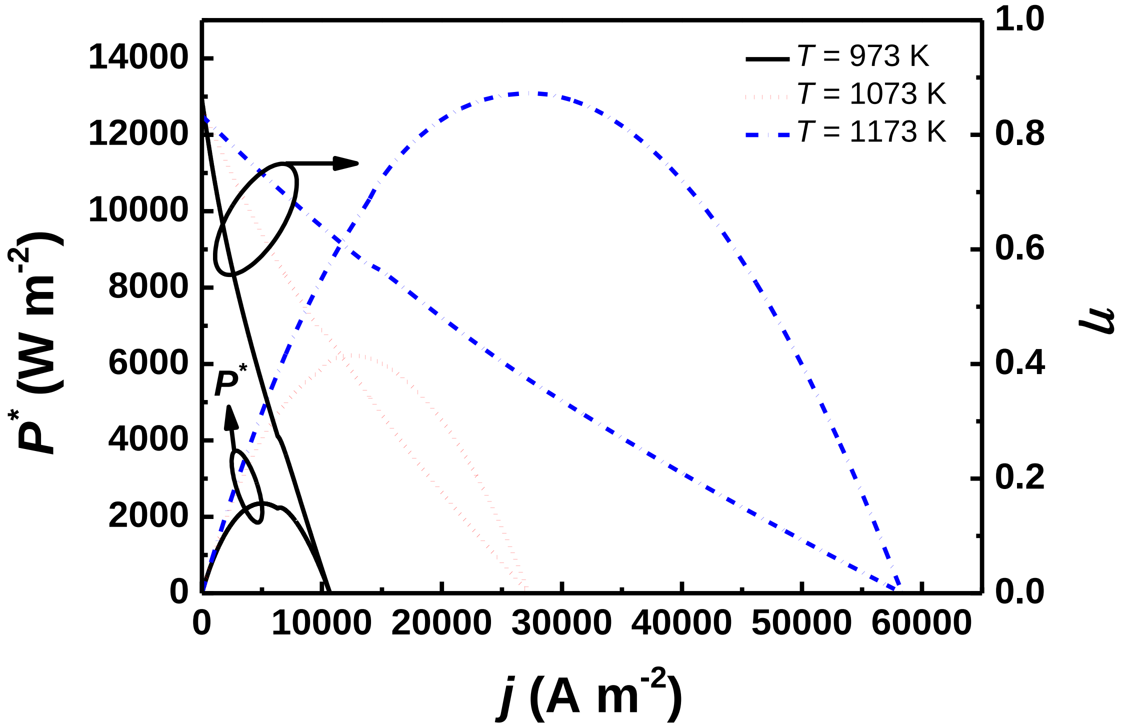
T = 973 K
T = 1073 K
T = 1173 K
P*
P* (W m-2)
η
j (A m-2)
0
2000
4000
6000
8000
10000
12000
14000
0.0
0.2
0.4
0.6
0.8
1.0
10000
20000
30000
40000
50000
60000

Fig. 6.

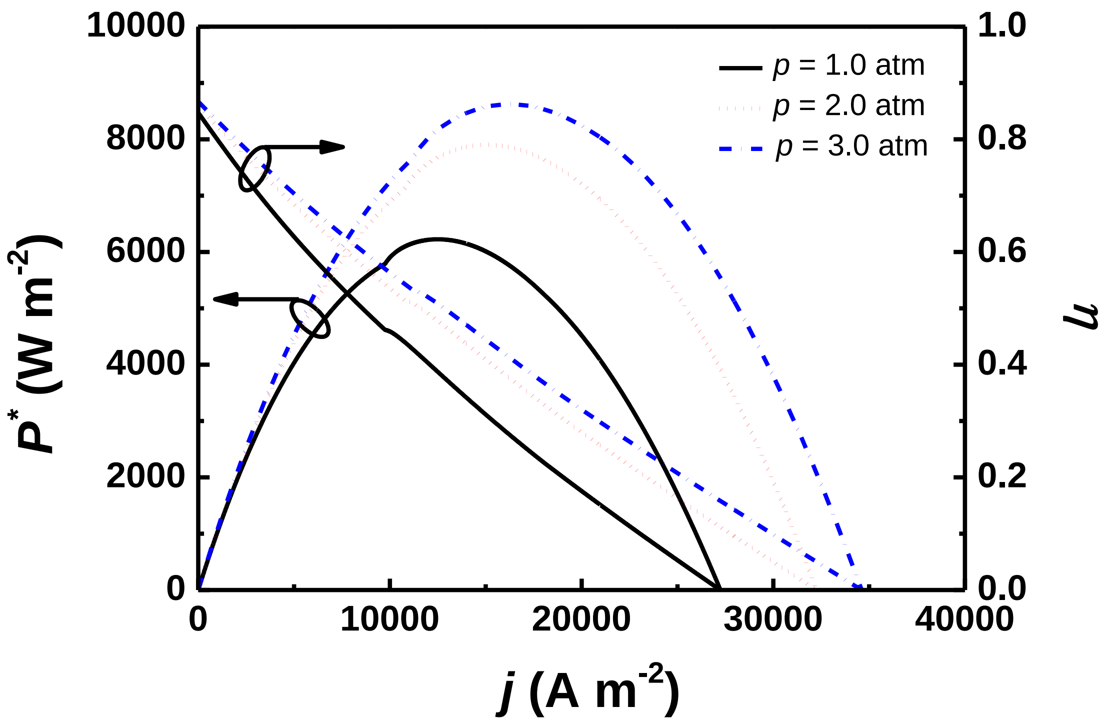

p = 1.0 atm
p = 2.0 atm
p = 3.0 atm
10000
8000
6000
4000
2000
0
1.0
0.8
0.6
0.4
0.2
0.0
0
10000
20000
30000
40000
P* (W m-2)
η
j (A m-2)

Fig. 7.

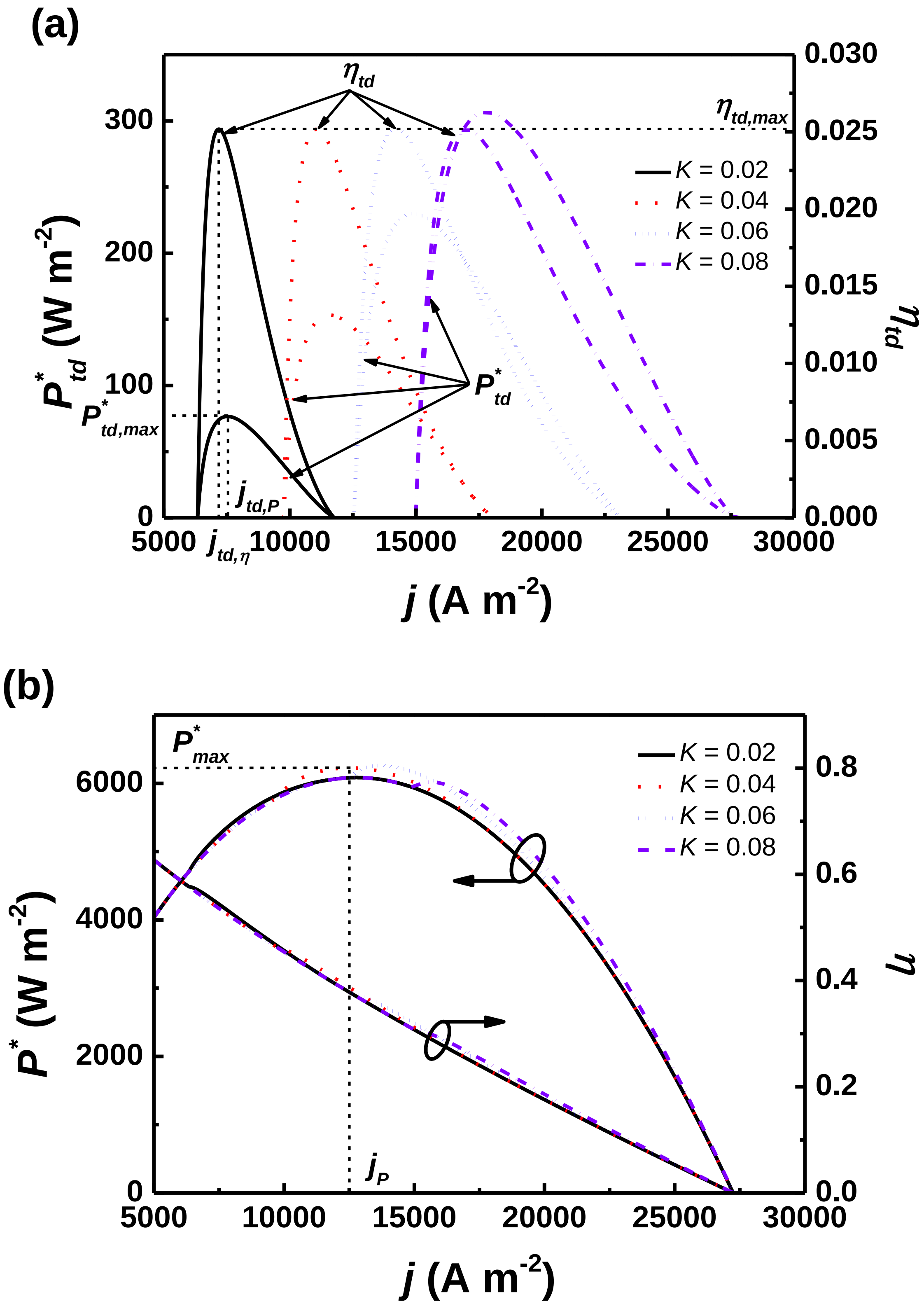

(a)
η_{td}
$\eta_{td,max}$
K = 0.02
K = 0.04
K = 0.06
K = 0.08
P^*_{td}
$P^*_{td,max}$
$j_{td,P}$
$j_{td,\eta}$
P^*_{td} (W m^{-2})
η_{td}
j (A m^{-2})
0
100
200
300
0.000
0.005
0.010
0.015
0.020
0.025
0.030
5000
10000
15000
20000
25000
30000
(b)
P^*_{max}
K = 0.02
K = 0.04
K = 0.06
K = 0.08
j_P
P^* (W m^{-2})
η
j (A m^{-2})
0
2000
4000
6000
0.0
0.2
0.4
0.6
0.8
5000
10000
15000
20000
25000
30000

Fig. 8.

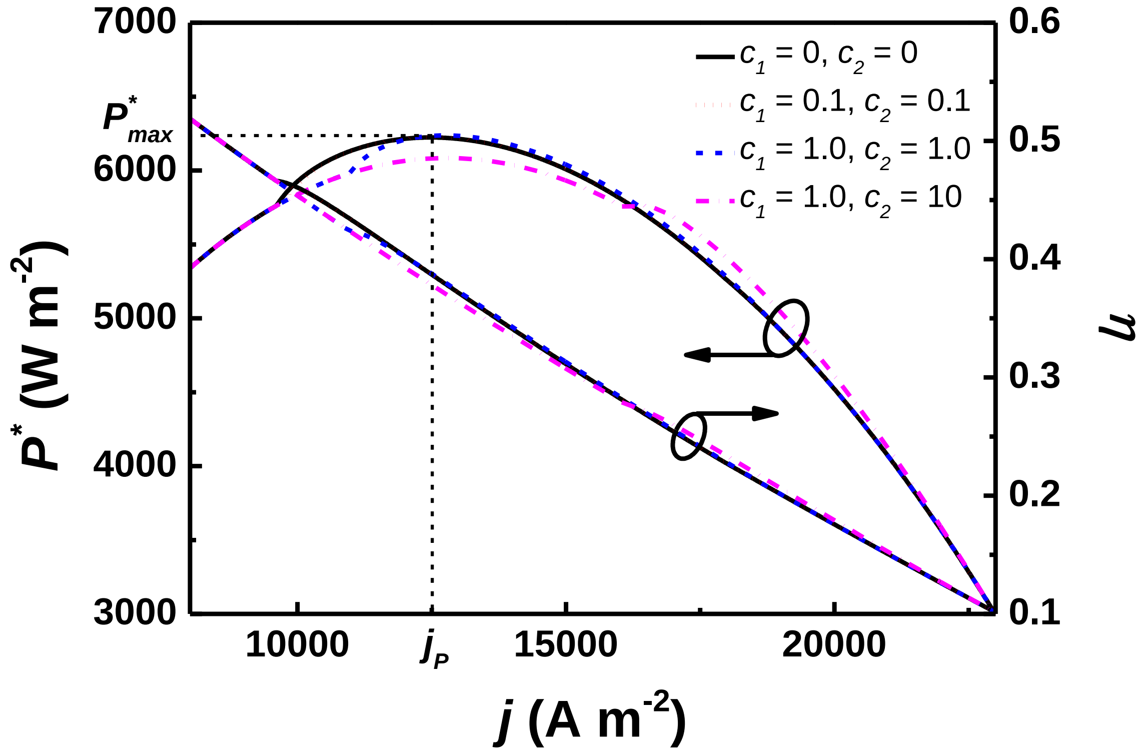
7000
6000
5000
4000
3000
P^*_{max}
P^* (W m^{-2})
0.6
0.5
0.4
0.3
0.2
0.1
u
10000
j_P
15000
20000
j (A m^{-2})
c_1 = 0, c_2 = 0
c_1 = 0.1, c_2 = 0.1
c_1 = 1.0, c_2 = 1.0
c_1 = 1.0, c_2 = 10